Estimating the mass of tephra accumulated on roads to best manage the impact of volcanic eruptions: the example of Mt. Etna, Italy

Luigi Mereu[1,2], Manuel Stocchi[1*], Alexander Garcia[1], Michele Prestifilippo[3], Laura Sandri[1], Costanza Bonadonna[4] and Simona Scollo[3]

[1]Istituto Nazionale di Geofisica e Vulcanologia, Sezione di Bologna, 40100 Bologna, Italy
[2]CETEMPS Center of Excellence, University of L'Aquila, 67100 L'Aquila, Italy
[3]Istituto Nazionale di Geofisica e Vulcanologia, Osservatorio Etneo, Sezione di Catania, 95015 Catania, Italy
[4]Department of Earth Sciences, University of Geneva, 1205 Geneva, Switzerland
[*]Now at Department of Earth and Geoenvironmental Sciences, University of Bari "Aldo Moro", 70125 Bari, Italy

Correspondence to: Luigi Mereu (luigi.mereu@ingv.it)

Abstract. During explosive eruptions a large amount of tephra is dispersed and deposited on the ground with the potential to cause a variety of damage and disruption on public infrastructure, such as road networks, which can require a rapid clean-up. The quantification of the tephra load is, therefore, of significant interest to reduce environmental and socio-economic impact, and for managing crises. Tephra dispersal and deposition is a function of multiple factors, including mass eruption rate, tephra characteristics (size, shape, density), top plume height, grain size distribution and local wind field. In this work we quantified the tephra mass deposited on the main road network on the east-southeast flanks of Mt. Etna (Italy), during lava fountains occurring in 2021. We focused this analysis on road connections of municipalities mostly affected by these events such as Milo, Santa Venerina and Zafferana Etnea. First, we analysed a sequence of 39 short-lasting and intense Etna's lava fountains detected by the X-band weather radar, applying the volcanic ash radar retrieval approach able to retrieve main eruption source parameters, such as mass eruption rate, top plume height, grain-size distribution of those events. When the radar measurements were unavailable for a specific event, we analysed images acquired both by the SEVIRI radiometer and by the visible and/or thermal infrared camera of the Istituto Nazionale di Geofisica e Vulcanologia, Osservatorio Etneo (Catania) to derive some ESPs. Second, we used those eruption source parameters as inputs to run two different numerical models, Tephra2 and Fall3D, and reproduce tephra dispersal and accumulation on the road network. Finally, we produce, for the first time, georeferenced estimates of tephra mass deposited on the whole road network of three municipalities, allowing to identify the main roads which have been mostly impacted by significant tephra accumulation, as well as to estimate the total mass of primary tephra that has been removed from roads and disposed. Such information represents a valuable input for quick planning and management of the short-term tephra load hazard for possible future Etna explosive events.

1 Introduction

30

The quantification of tephra mass deposited on the ground following a volcanic explosive eruption of a specific intensity is still today a key information little known in literature. In fact, tephra dispersal and fallout is by far the most widespread volcanic hazard affecting both local and distal areas (Jenkins et al. 2015; Barsotti et al., 2018; Bonadonna et al. 2021b) including impact on public health (Baxter, 1990; Horwell and Baxter, 2006), roofs/building collapse (Spence et al., 2005),

35 poor visibility conditions (Blong, 1996), dangerous road conditions (Wilson et al., 2012; Jenkins et al., 2014; Blake et al., 2017), contamination of water reservoirs and vegetation (Wilson et al., 2012; Ágústsdóttir, 2015), damages to electrical infrastructure (Bebbington et al., 2008; Wardman et al., 2012; Wilson et al., 2012, Dominguez et al., 2021), transportation system disruptions (Casadevall, 1994; Guffanti et al., 2009; Wilson et al., 2012), and impact on telecommunication networks (Wilson et al., 2012). Even tephra associated with relatively small intensity eruptions may induce various disrupting effects

40 on transport infrastructure such as aeroplane engine failure and visibility reduction during both primary tephra fall and ash remobilisation (Sarna-Wojcicki et al., 1981; Bonadonna et al., 2021b; Johnston and Daly, 1995; Wilson et al., 2014). In particular, tephra accumulation, although not causing significant physical damage on the road network, can cause wide disruption including reduction of skid resistance, obscuration of road markings and damage to car air filters (Blake et al., 2016, 2017). Tephra particles are also very abrasive with the degree of abrasiveness dependent on the hardness of the

45 material forming the particles and their shape and angularity (Blong, 1984; Johnston, 1997; Labadie, 1994; Heiken et al., 1995; Miller and Casavedall, 1999; Gordon et al., 2005; Wilson et al., 2012; Blake et al., 2017). Road networks are critical for society under normal operating conditions and especially during emergencies (e.g. Bonadonna et al. 2021a; Hayes et al. 2022). During volcanic eruptions, routes may be required for the evacuation of residents, to allow emergency services and civil protection personnel to access the affected areas. Road network is also crucial for both immediate and long-term

50 recovery, including clean-up and disposal of pyroclastic material, and restoration of services and commerce (Blake et al., 2017).

In this work, for the first time, we try to quantify the tephra mass accumulated on the road network of east and south-east sectors of Etna that were more affected during the sequence of explosive events of 2021. Usually, the eruptive sequences at Etna are characterised by short-lasting explosive events, with duration of few hours and sometimes occurring every few days

55 or several times a day (Calvari et al., 2018; Andronico et al., 2021; Calvari et al., 2022a). Most studies on exposed critical infrastructure have generally focussed on larger events and tephra-fallout accumulations greater than 10 kg/m^2 (Wilson et al., 2012, Blake et al., 2017; Scollo et al., 2013). However, areas around Etna are more frequently impacted by smaller accumulation (Scollo et al., 2013). Limited quantitative data available for explosive activity have hampered a reliable quantification of the impact of the tephra deposition at Etna. To investigate its impact on road networks and better

60 characterise its behaviour, we analysed a sequence of several lava fountains occurred between February 2021 and October 2021, focusing our analysis only to 39 events which generated volcanic plumes dispersed by wind mostly towards the east-southeast flanks of the volcano (direction between 90 degrees and 130 degrees from North). These episodes began at the

South East Crater (SEC) as initial Strombolian activity that, with time, evolved in lava fountain activity, also named paroxysm, accompanied by the formation of sustained eruptive columns of about 10-15 km above sea level (Calvari et al.,

65 2022b).

Remote sensing is routinely used for monitoring the eruptive activity of Etna; the Istituto Nazionale di Geofisica e Vulcanologia, Osservatorio Etneo (INGV-OE) runs a network of different remote sensing sensors both ground-based (such as thermal infrared and visible cameras) and satellite-based sensors (Scollo et al., 2019). An X-band weather radar located in Fontanarossa airport (Catania), which is part of the monitoring network of the Italian Department of Civil Protection (DPC)

70 allows to monitor and analyse the Etna's eruptions as well (Marzano et al. 2020; Mereu et al. 2020). Using those sensors, we can observe in almost all the cases the time evolution of explosive activity and characterise it quantitatively in terms of MER and HTP. These two parameters are among the main input variables for advection-dispersion models, such as Tephra2 and Fall3D (Bonadonna et al., 2005; Scollo et al., 2008; Biass et al., 2017; Costa et al., 2006; Folch et al., 2009, 2020), which have been used in this work to simulate the tephra dispersion and to calculate the deposit load at the ground. For each of the

75 39 events we estimate the deposited tephra on the road network in order to identify the roads mostly exposed to tephra accumulation and evaluate the ground mass load that had to be removed. Moreover, analysing the simulations of both models, we investigate their sensitivity to variations of tephra granulometric characteristics and to assess uncertainties. The numerical output from a single simulation is a georeferenced map of tephra load, useful to analyse the impact of deposited tephra fallout on roads (Scollo et al., 2009; Scollo et al., 2013, Costa et al., 2012, Bonadonna et al., 2005, Barsotti et al.,

80 2018, Bonadonna et al. 2021).

Quantifying the expected amount of tephra accumulated in the road network, considering both single eruptions and the cumulative effect of a sequence of eruptions, theoretically allows us to identify the critical roads that have been mostly affected by the impact of tephra fallout in a given period of time. In this way it is possible to provide a quantification of the expected mass that potentially needs to be removed and disposed of after each event and during a sequence of eruptions. In

85 addition, in this way it is possible to envisage in advance plausible costs to effectively plan the cleaning operations, as well as to evaluate the consequent losses in various sectors directly and indirectly involved. Moreover, clean-up operations can be expensive due to extensive areas involved by the tephra deposits and due to potentially large volumes of tephra needing to be removed (Hayes et al., 2015; Magill et al., 2006). In this perspective, our retrospective analysis considering Etna's eruptions in 2021 is done to assess the feasibility to implement this kind of procedure in future events for planning tephra clean up and

90 disposal operations during future Etna's explosive activities.

The work is organised as follow: ground- and satellite-based sensors data, and main eruption source parameters (ESPs) retrieved from them, are discussed in sections 2; the methodology employed to analyse models' results is presented in section 3; the validation of results with respect to previously published data for a specific event (February 28th, 2021) is presented in section 4; output from modelling is discussed in section 5 and finally, the conclusive remarks are in section 6.

95

2 Methods

2.1 Sensors and outputs

We select a set of 39 Etna eruptions, listed in the first three columns of Table 1, characterised by a tephra plume dispersed
towards east-southeast flanks of Etna, and observed by different sensors listed below:

a) X-band Weather Radar (XWR), located in the airport of Catania, 32 km at SSE Etna summit craters, Fig. 1. The scanning
agility in elevation and azimuth of this sensor allows it to probe the tephra cloud in any weather condition and both during
the day and night (Mereu et al., 2022, 2023; Montopoli, 2016; Vulpiani et al., 2016). Applying the Volcanic Ash Radar
Retrieval (VARR) methodology (e.g. Marzano et al., 2012, 2020; Mereu et al., 2015, 2020) to measured radar reflectivity
factor, we estimate: i) the top plume height H_{TP} (km) above sea level, which is the maximum height reached by the eruption
column, that is the maximum altitude of the radar-detected volume above the volcanic vent contaminated by the minimum
detectable tephra concentration; ii) the mass eruption rate Q_M (kg/s), that is estimated by the time-space variation of tephra
concentration detected above the Etna summit probing the volcanic plume; iii) integrating the latter parameter in time we
retrieve the total erupted mass TEM (kg), which is the total mass of pyroclastic material erupted during the explosive event.

b) Etna Catania Visible camera (ECV), located in Catania about 30 km from Etna summit craters (Scollo et al., 2019, Fig. 1),
allows to monitor the altitude of dispersed plume during the light hours when the visibility is not compromised by the
meteorological cloud cover. In this way, we can derive the time sequence of H_{TP}.

c) Spinning Enhanced Visible and InfraRed Imager (SEVIRI), on board of Meteosat Second Generation (MSG) satellites, is
a multispectral radiometer which produces daytime brightness temperature (BT) images with 3 km resolution. Selecting the
BT along the Etna summit in the channel of 10.8 μm, that is more sensitive to the tephra dielectric signature, we infer H_{TP}
looking for the altitude in which the detected BT can be found in the temperature profile as a function of altitude derived
from the hydro-meteorological service of Agenzia Regionale Prevenzione e Ambiente (ARPA) in Emilia Romagna (Scollo
et al., 2009; Romeo et al., 2023).

d) Etna Nicolosi Thermal (ENT) infrared camera, located in Nicolosi at about 15 km from Etna summit (Fig. 1), which
measures the thermal activity associated with lava fountains. It's worth highlighting that when the radar measurements were
not available and the volcanic plume was not easily detectable by the satellite sensor or by the visible calibrated camera,
analysing the ENT images we have identified the Incandescent Jet Region (IJR), which is a proxy of the lava fountain height.
As described in Mereu et al., (2020), the time sequence of maximum height of IJR area can be converted in exit velocity
v_{ex}(m/s) of pyroclastic material, using the Bernoulli equation under specific approximations: i) most of the pyroclastic
material is sufficiently large to be considered as accelerated projectiles confined in this IJR; ii) atmospheric density
variations and drag effects are negligible. Assuming a trustworthy value of tephra-gas mixture density and of surface vent,
we can deduce Q_M applying the surface flow approach (SFA) described in Marzano et al., (2020) and Mereu et al., (2022).
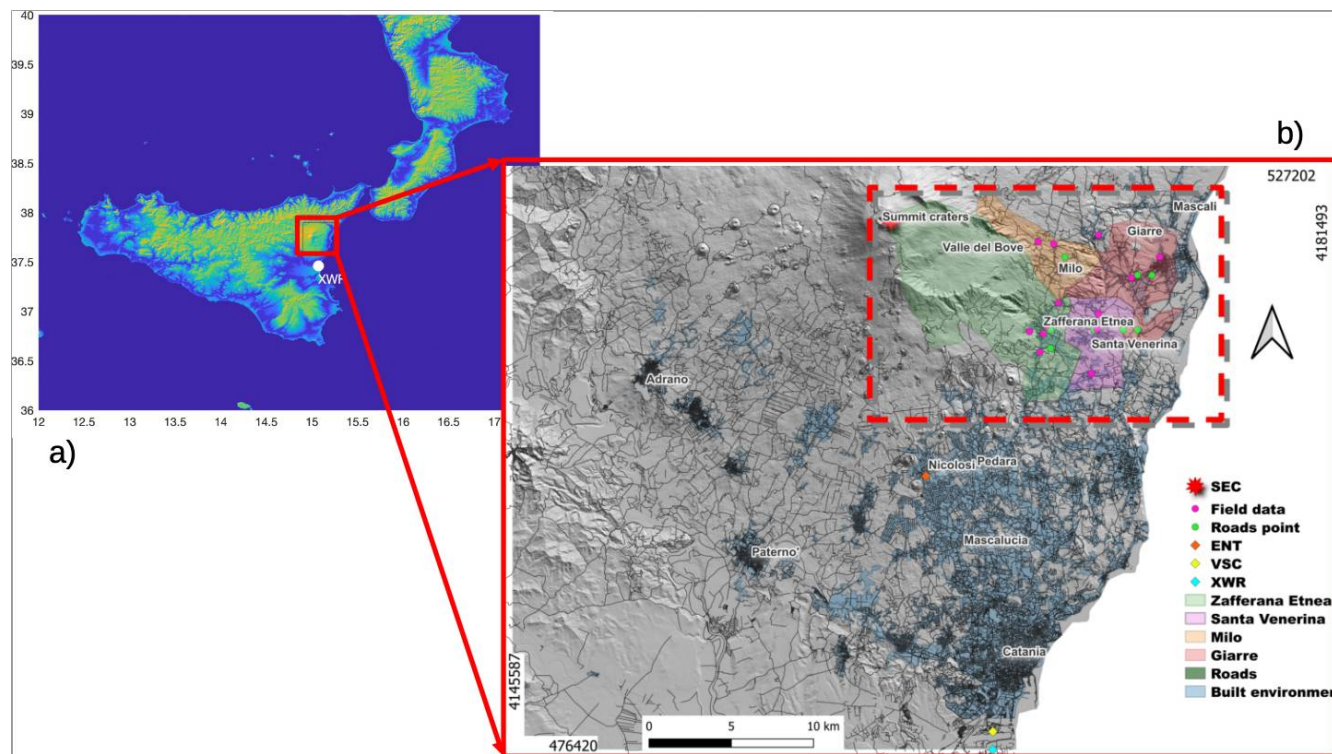
4

Figure 1: (a) Map of South Italy (Sicily and Calabria), with the red square showing the Etna area framed in the right panel; (b)
georeferenced map of road network (dark lines) of the Etna volcano area (shapefiles with the road data is publicly available from
the Regione Sicilia website: https://www.regione.sicilia.it/). The UTM coordinates (area 33S) are shown in the lower-left part and
in the upper-right part of the picture, respectively. The areas of four municipalities, of which three of these under examination and
the built environment are highlighted with different colours, whereas each sensor, field data and road points are identified by
coloured symbol as listed in the legend in the right side: ground-based sensors employed in this work (the visible camera VSC, the
thermal infrared camera ENT and the X-band radar XWR); the South East Carter SEC; 14 field data as derived by Pardini et al.
(2021); 8 road points. The rectangle highlighted with the dotted red line identifies the area examined and focused in Figs. 3 and 6.
Made with QGIS.

The complete ESPs dataset for each of the Etna events considered in this study is derived by processing data from the
measurements previously described. Usually, real-time ESPs estimation is not always easy, mainly in the starting phase, and
not fully automated, increasing in this way the uncertainty in the short-term forecasting the plume dispersal (Scollo et al.,
2008). We derive some qualitative information about the eruption, such as plume height from the VONA (Scollo et al.,
2019, Corradini et al., 2018), the presence of tephra, start and end time of the Strombolian and lava fountain activities from
bulletins and reports available in the web-site of INGV-OE (www.ct.ingv.it). On the other hand, each sensor previously
described allows us to measure some features of the lava fountains, which need further elaborations to obtain the ESPs. In
this work, H_{TP} (km) and Q_M (kg/s) quantities are directly derived by processing XWR measurements. When it was not

possible to determine H_{TP} from XWR, ECV frames or SEVIRI data, we used the ENT images to retrieve the Q_M estimates applying the SFA (Marzano et al. 2020; Mereu et al., 2022). Integrating the SFA in time, we obtain TEM (kg), whereas applying the empirical relation of Mastin et al. (2009), which links Q_M to HTP, we get the H_{TP} above the Etna summit crater (which is located about 3357 m above sea level). We used the inverse Mastin equation in those cases where the H_{TP} was

150 derived from VSC or SEVIRI imagery to obtain the Q_M time sequence. The starting and ending time for each Etna explosive eruption can be straight inferred selecting the ends of time range from: i) Q_M estimates XWR-derived, where $Q_M > 5 \ 10^5$ kg/s; ii) temporal range where ENT camera identifies the lava fountaining feeding the explosive phase; time range in which a quick development of the volcanic cloud is observed by iii) ECV frames or iv) SEVIRI images.

The winds field used to feed the ash dispersion models used in this work are derived from the European Centre for Medium-

155 Range Weather Forecasts (ECMWF) ERA5 reanalysis (https://www.ecmwf.int/en/forecasts/datasets/reanalysis-datasets/era5). For each case study, we compute the vertical mean wind velocity between the Etna summit craters and the maximum value of H_{TP} sequence.

The grain-size distribution usually refers to the volcanic particle size, indicated by the relation $\phi = -\log2 (D)$, where D stands for sphere-equivalent mean diameter (measured in mm). The ϕ refers to the whole deposit, assumed as a Gaussian

160 distribution characterised by a maximum, minimum, median and standard deviation, as available in literature. In order to consider all possible cases, in this work we vary the median ϕ value between -1 to +1 with a step of 0.5. The georeferenced location and the elevation of the SEC are considered to complete the set of input parameters used, as listed in the Table 1. It's worth noting that for each event listed in Table 1, known the coordinates of the vent in easting (500024.03 m) and northing (4177699.5 m), we assume a ϕ with maximum, minimum and standard deviation values equal to -6, 10 and 3,

165 respectively; we repeat each simulation, varying the median ϕ values, so that we obtain a total of 195 simulations from each numerical model.

Table 1. Input parameters used for setting the numerical dispersion model Tephra2 and Fall3D: starting time and ending time of paroxysm (dd:mm:yy, hh:mm), duration Δt (s), top plume height H_{TP} (m) above sea level (a.s.l.) and above volcano vent (a.v.v.),

170 **total erupted mass TEM (kg).**

START TIME Date T0 UTC	END TIME Date T=T0+Dt UTC	Δt [s]	H_{TP} (a.s.l) [m]	H_{TP} (a.v.v.) [m]	TEM [10^7 kg]
17/02/21 23:40	18/02/21 01:20	6000	9300	5943	18
19/02/21 08:40	19/02/21 10:30	6600	10000	6643	29
28/02/21 07:50	28/02/21 09:50	7200	11900	8543	250
07/03/21 06:20	07/03/21 07:50	5400	11600	8243	110

12/03/21 05:50	12/03/21 10:50	18000	10500	7143	175
14/03/21 23:20	15/03/21 02:20	10800	10957	7600	540
17/03/21 02:50	17/03/21 05:10	8400	6300	2943	22
19/03/21 08:40	19/03/21 10:20	6000	10400	7043	98
19/05/21 03:00	19/05/21 04:30	5400	5000	1643	0.09
22/05/21 20:20	22/05/21 22:40	8400	11057	7700	445
24/05/21 20:30	24/05/21 22:45	8700	11000	7643	468
28/05/21 06:20	28/05/21 07:50	5400	10857	7500	0.4
28/05/21 18:10	28/05/21 21:10	10800	10757	7400	486
30/05/21 03:00	30/05/21 06:00	10800	7500	4143	46.9
02/06/21 08:10	02/06/21 10:50	9600	7600	4243	13.2
04/06/21 16:40	04/06/21 18:40	7200	7500	4143	10
12/06/21 18:30	12/06/21 19:10	2400	9000	5643	17.7
14/06/21 21:40	14/06/21 22:30	3000	6300	2943	56
16/06/21 10:30	16/06/21 13:00	9000	8000	4643	15.8
17/06/21 22:40	17/06/21 23:55	4500	12457	9100	290
20/06/21 22:40	21/06/21 00:40	7200	10900	7543	18
22/06/21 03:30	22/06/21 04:20	3000	8000	4643	11.8
23/06/21 02:00	23/06/21 03:40	6000	7300	3943	77
23/06/21 17:40	23/06/21 19:00	4800	11500	8143	120
24/06/21 09:20	24/06/21 11:00	6000	12200	8843	4.2
25/06/21 18:20	25/06/21 19:40	4800	10664	7307	4.8
25/06/21 00:30	25/06/21 02:40	7800	10616	7259	230
26/06/21 15:20	26/06/21 17:20	7200	9000	5643	22
27/06/21 08:50	27/06/21 10:00	4200	10000	6643	72.9
28/06/21 14:30	28/06/21 15:40	4200	10000	6643	68.8
01/07/21 23:40	02/07/21 01:40	7200	11109	7752	396
04/07/21 15:00	04/07/21 17:50	10200	8200	4843	8.8
06/07/21 22:00	06/07/21 23:45	6300	10000	6643	190
20/07/21 06:20	20/07/21 08:30	7800	11800	8443	79
31/07/21 21:00	31/07/21 23:50	10200	11000	7643	309
09/08/21 02:00	09/08/21 04:40	9600	12000	8643	140
29/08/21 16:40	29/08/21 18:00	4800	9000	5643	13.1
21/09/21 07:30	21/09/21 09:20	6600	10900	7543	47
23/10/21 08:40	23/10/21 11:30	10200	12300	8943	240

2.2 Models

2.2.1 Modelling tephra fallout

In this study, we simulate the transport, dispersal and deposition of tephra with two different numerical models: Tephra2 and Fall3D. We run both models on a grid covering the area (14.5° lon, 37° lat) and (16° lon, 38.5° lat) with a spatial resolution

175 of 500 m. Tephra2 allows to evaluate the ground tephra deposition employing the advection-diffusion theory (Bonadonna et al. 2005; Bonadonna et al., 2006; Connor and Connor, 2006; Volentik et al. 2009; Biass et al. 2016, 2017) taking as input: H_{TP}, TEM, ϕ, the density of lithics and juveniles (volcanic particles released from the column, which varies widely from ~500 kg/m^3 in highly vesicular clasts to ~2700 kg/m^3 in dense ones), the diffusion coefficient (K), which accounts for atmospheric processes including atmospheric diffusion and cloud gravitational spreading, the fall time threshold (FTT), an

180 empirical threshold that defines the transition between two different laws of atmospheric diffusion, the plume ratio (PR), factor describing the mass distribution in the plume. Fall3D models both the particle concentration in the atmosphere (i.e. tephra cloud evolution) and the particle loading at ground level, based on a 3-D time-dependent Eulerian scheme (Costa et al., 2006; Folch et al., 2009). The model is based on the advection-diffusion-sedimentation equation able to evaluate a turbulent diffusion given by the gradient transport theory, considering as input a wind field obtained from a meteorological

185 model and using a source term derived from buoyant plume theory. This methodology has the potential capability to follow the evolution of particle concentration during an eruption, but the main inconvenience is the cost in computational time (Costa et al., 2006). Fall3D uses the same ESP's inputs listed in Table 1, but instead of TEM, it considers Q_M. Fall3D simulations have been performed thanks to the computational resources of the ADA cluster of Istituto Nazionale di Geofisica e Vulcanologia, Sezione di Bologna. Figure 2 shows the simulated tephra load (kg/m^2) maps for two among the largest-TEM

190 eruptions (10^8 kg and 10^9 kg), assuming a ϕ=0.5. In particular, we plot in Figure 2.a and Figure 2.b the event of 17 February 2021 and in the panels c)-d) the event of 23 October 2021, as obtained from Tephra2 and Fall3D, respectively. Generally, we note a greater spreading of tephra deposition to the ground simulated by Tephra2 with respect to Fall3D. Isomass contour lines are shown with grayscale, from black for values lower than 10 kg/m^2 to light white for values greater than 5 10^3 kg/m^2.
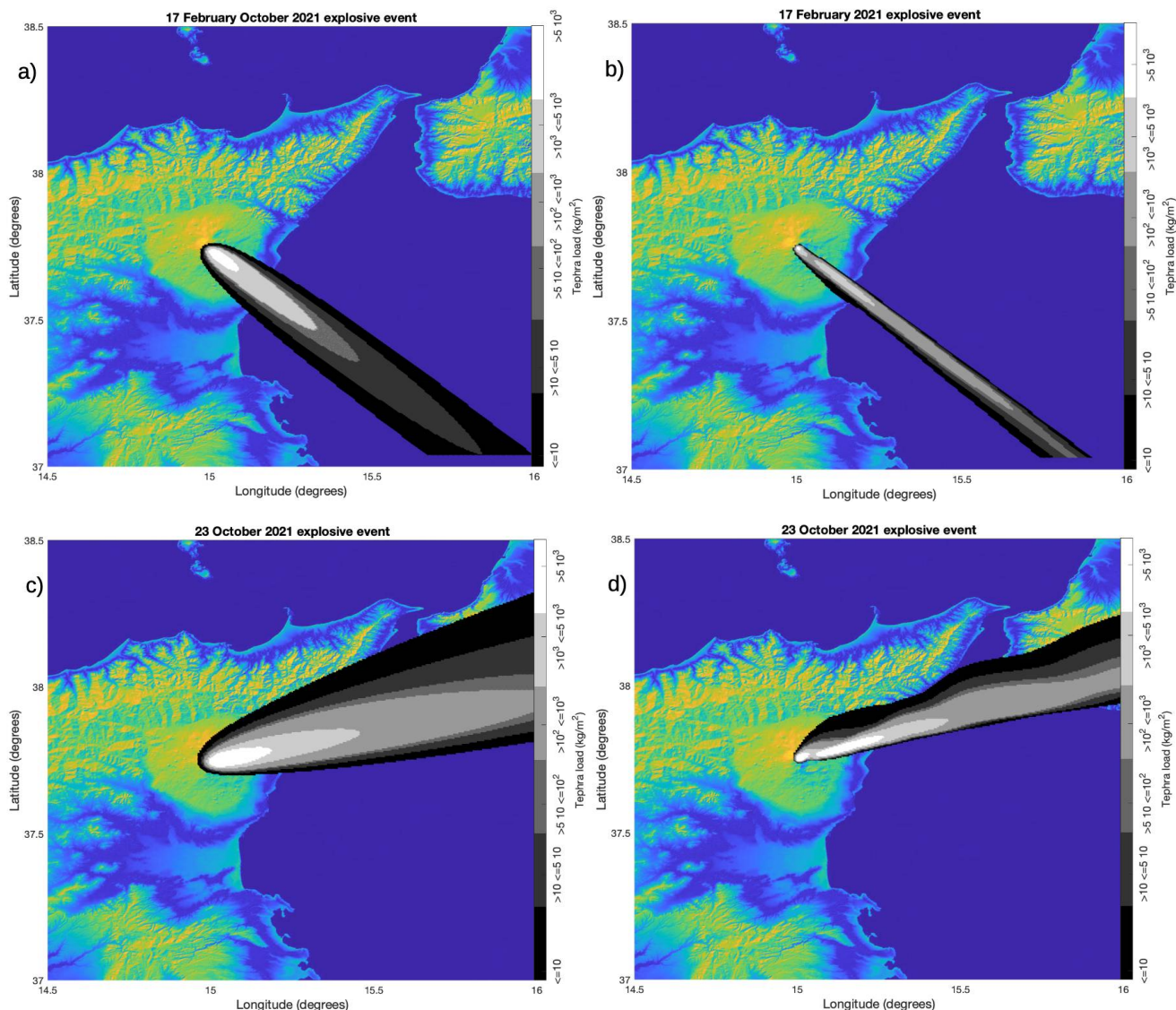
195

Figure 2: Maps of tephra load (kg/m²) for the Etna lava fountain event of 17 February 2021 (a)-b)) and of 23 October 2021 (c)-d)), using the Tephra2 (a)-c)) and Fall3D (b)-d)) models. The tephra deposition is plotted as uniform iso-mass coloured in function of defined levels of tephra. The colour scale is the same in all panels.

200 **2.2.1 Calculating the tephra load and mass on the road network**

Both numerical models generate output files in netCDF format (e.g. https://www.unidata.ucar.edu/software/netcdf/) containing the geo-referenced data in UTM coordinates (zone 33-S for Etna) with a spatial resolution of 500 m, and the simulated tephra load (kg/m²) on the ground. Since our main interest in this work is to calculate the tephra load in the road network, we increase the resolution of the tephra load data to 5 m using linear interpolation. Afterwards, we use the

9

Quantum Geographical Information System (QGIS) tool to determine the intersection between the downscaled tephra load data and the areas covered by the road network. While the tracks of road network in the study area is publicly available (geospatial vector data in shapefile format, as shown in Fig. 1, from the Regione Sicilia; website https://www.regione.sicilia.it/), an estimate of the road's area/width is not available. In order to estimate the roads' area, we selected a sample of the most common roads in the study area (which are in general composed of two carriageways/road) and measured the width, obtaining an average value for the road width of 6 m. This result is in agreement with the expected values according to the prescriptions by the law in Italy (Art. 2 del Testo Unico), which defines the carriageway width for urban and extraurban roads ranging from 2.8 m and 4 m.

The case study is focused on the road networks located within the municipal area of Milo, Santa Venerina and Zafferana Etnea towns. For a given road segment we calculate the relative road area (m^2) and then using the tephra load (kg/m^2) we calculate the total mass (kg) deposited on each road segment. Figure 3 (which covers the area in the rectangle shown with a dotted red line in Fig. 1) shows the simulated tephra load (kg/m^2) on the geo referenced road network within the Milo (light orange area), Santa Venerina (light pink area) and Zafferana Etnea (light green area) municipalities for the event on 28 February 2021; in both plots the tephra load is represented in red scale for selected threshold levels (as shown in the legend), using Tephra2 (Fig. 3a) and Fall3D (Fig. 3b) models.
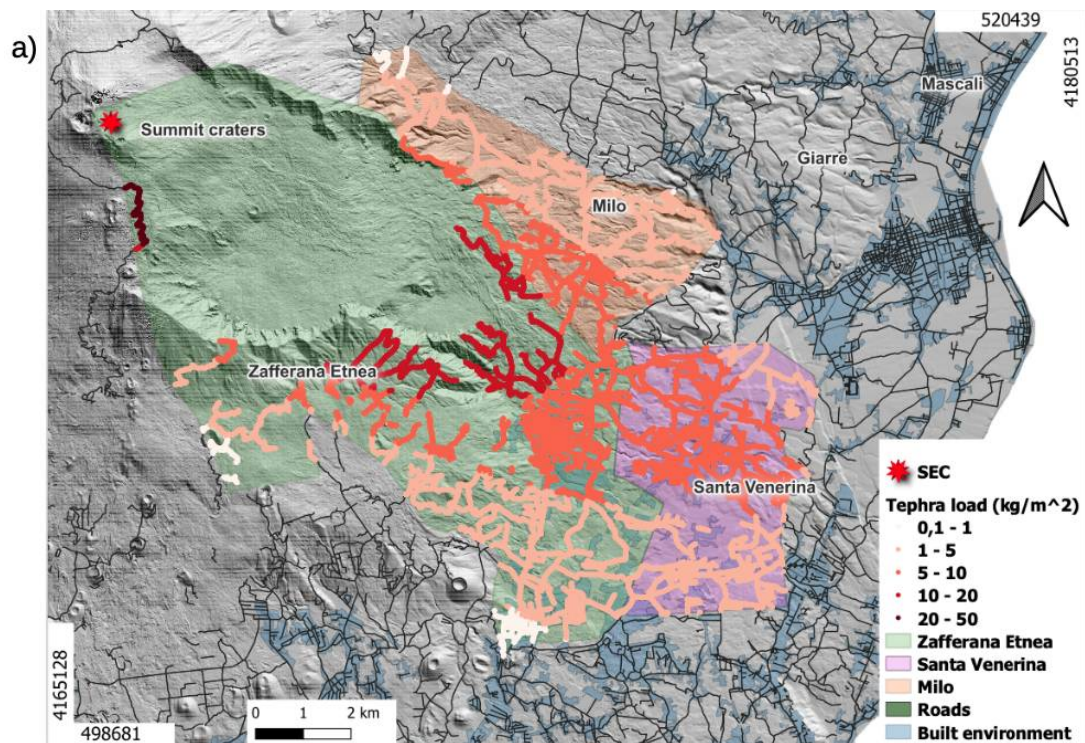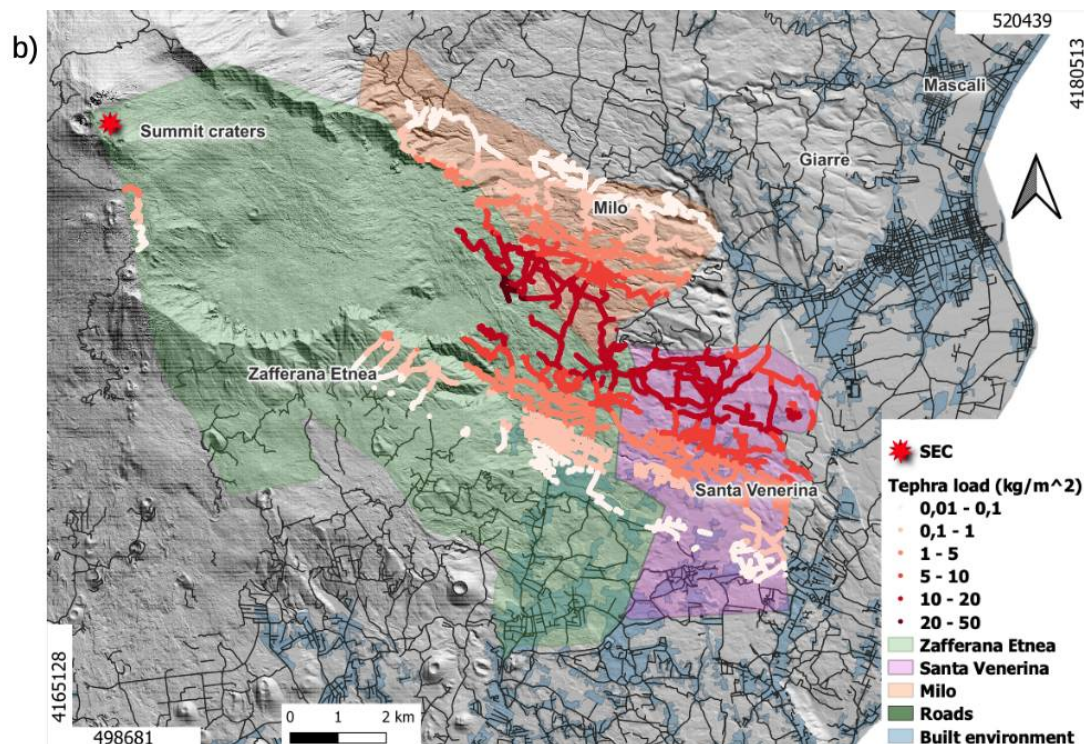
Figure 3: Tephra load (kg/m²) on the road network of Milo, Santa Venerina and Zafferana Etnea municipalities computed for the Etna explosive event on 28 February 2021, assuming φ =0.5 and using both Tephra2 (a) and Fall3D (b) models. The tephra deposits in the road graph are shown in red scale coloured in function of the tephra load values. Georeferenced map of road network (dark lines) of the Etna volcano area (shapefiles with the road data is publicly available from the Regione Sicilia website: https://www.regione.sicilia.it/). Made with QGIS.

3 Results

3.1 Validation: case study on February 28, 2021

In order to validate the results obtained in this study, we focus our attention on the case study of the event on 28 February 2021, which has been observed by the XWR and analysed by Pardini et al. (2021). Table 2 shows the coordinates (longitude, latitude) of 14 points in which field measurements of tephra load are available (from literature, e.g., Pardini et al., 2021) in the selected municipalities (see Figure 1); Table 2 shows also the results of tephra load derived from the Tephra2 and Fall3D models, fixing the φ to 0.5. The XWR retrievals are obtained considering the tephra load rate (kg/m² s) related to first four elevations, which is equal to a few km of altitude with respect to the ground, and integrating it for the whole time sampling of the radar (s). In this way we can retrieve the tephra load (kg/m²) related to the whole lava fountain. We observe the same order of magnitude of tephra load derived from the Tephra2 model, the XWR and the ground field data (Pardini et al., 2023),

11

whereas a difference of one order of magnitude among the results of Fall3D and field data is shown in different cases. These
240 are mainly due to different dispersal settings of the numerical model.

Table 2. Etna eruption on February 28, 2021: tephra load (kg/m^2) derived on 14 field data, each one identified by the latitude and longitude, as deduced by Pardini et al. (2021), and in the same points as derived by Tephra2 and Fall3D models (fixing φ =0.5) and retrieved by XWR.

Coordinates (degrees)		Tephra load (kg/m^2)			
Longitude	Latitude	Tephra2	Fall3D	XWR	Field data
15.102649	37.677930	5.0	0.0	2.4	1.0
15.095485	37.689185	9.0	0.0	4.1	3.3
15.104990	37.688067	8.9	0.2	4.3	3.3
15.107469	37.692398	8.7	1.1	7.6	6.2
15.115397	37.704832	9.1	16.8	8.4	4.7
15.117104	37.722241	4.0	1.9	6.7	4.3
15.112271	37.737129	1.6	0.0	3.5	2.4
15.101504	37.738418	1.6	0.1	3.5	2.1
15.143073	37.742075	0.2	1.7	1.6	0.1
15.165928	37.718516	1.3	0.0	2.3	1.5
15.141991	37.690479	6.4	10.5	3.4	3.9
15.138243	37.666113	4.4	0.0	1.0	1.0
15.142994	37.698936	5.6	13.1	3.1	4.6
15.185512	37.729891	0.2	1.4	0.5	0.5

260 Assuming the width of 6 m for each road, we convert the tephra load to tephra mass (kg) for the event of 28 February 2021, assuming φ equals 0.5. We selected few roads, characterised by greatest extension, for each municipality: Via Bellini and Corso Italia in Milo; via Mazzini, via Galimberti and via Stabilimenti in Santa Venerina; via Libertà, via Zafferana Milo and via delle Rose in Zafferana Etnea. We summarise in Table 3 the total tephra mass for streets of Milo, Santa Venerina and Zafferana Etnea as derived from Tephra2 and Fall3D models.

265 The total mass computed for the selected roads in Milo by Tephra2 and Fall3D shows a comparable order of magnitude (10^7 kg), whereas for two selected roads in Zafferana Etnea reveals a disagreement of one order of magnitude. However, the

values computed for all municipalities show a maximum variability between more or less five times the tephra deposit collected on the ground (Scollo et al., 2007). The last three rows in Table 3 show the total mass computed on the whole road network of the three municipalities, highlighting the comparable results (same order of magnitude of about 10^9 kg). It is worth noting that the total mass derived from Tephra2 in Zafferana Etnea municipality is four times larger than the total mass derived from Fall3D. This variability can be observed in Fig. 3 (not all roads are affected by tephra load as shown in the panel b) of Fig. 3) and can be attributed to specific dispersal laws implemented in the model. It is worth noting that during a typical Etna explosive event, a total tephra mass of a few kg can accumulate only on a few streets of three municipalities. Generally, the tephra deposition can be extended over time even after the end of the explosive activity. This last aspect is strictly connected to the intensity of the explosive event and therefore to the amount of pyroclastic material erupted as well as to the wind dispersal.

Table 3. Total tephra mass (kg) computed on main roads selected of Milo, Santa Venerina and Zafferana Etnea for the Etna eruption on 28 February 2021 as derived from the results obtained using Tephra2 and Fall3D models (fixing ϕ=0.5). The total mass on the road network of Milo, Santa Venerina and Zafferana in the last three rows.

| Lava fountains on 28 February 2021	Total tephra mass (10^7 kg)	
Location	**Tephra2**	**Fall3D**
Milo-Via V. Bellini	2.6	1.4
Milo-Corso Italia	1.6	1.9
S. Venerina-Via G. Mazzini	0.2	0.1
S. Venerina-Via D. Galimberti	10.6	10.7
S. Venerina-Via Stabilimenti	0.5	0.9
Zafferana E.-Via Libertà	1.8	0.5
Zafferana E.-Via Zafferana Milo	3.0	4.3
Zafferana E.-Via delle Rose	1.1	0.3
Total mass on the municipality's road network (10^7 kg)		
Milo	185.4	143.3
Santa Venerina	141.3	157.2
Zafferana Etnea	719.0	180.2

3.2 Tephra mass on specific road-ponits

We investigate how tephra loads, derived from both models, can be used to assess the accumulated tephra mass on the road network for the selected municipalities, assuming a cell size of 5 x 5 metres in the interpolated tephra load map. It is worth

285   noting that deposited tephra generates a type of disruption on main roads defined with regards to kilometres of roads potentially exposed to critical driving conditions. The location of the Etna volcano, in the northernmost tip of the Sicily, together with the prevailing westerly and north westerly winds at high altitude favours the tephra fallout and dispersal mainly toward the east (31%) and southeast (35%) Etna flanks, and the nordwest (29%) and only (6%) at south, as deduced from the wind analysis during 39 eruptive events occurred in 2021. First, we evaluate the deposited tephra mass with both models,

290   selecting eight road-points on different roads of Milo, Santa Venerina (abbreviated in Sven), Zafferana Etnea (abbreviated in Zaff) and Giarre municipalities: provincial roads (SP41, SP92, SP8 and SP59); highway (E45); state road (SS114). We also consider the road-points (E45 and SP114) selected into the municipality of Giarre to increase the set of road-points on the southeast flank of Etna. All the selected points are shown in Fig. 1. In Figure 4 we show the time cumulative tephra mass for different median ϕ values at specific points in the selected roads, as computed by Tephra2 (Fig. 4.a)) and Fall3D (Fig. 4.b)).

295   Each road-point is identified by the same coloured line and symbol. Generally, increasing the median ϕ increases the deposited tephra mass and vice versa. Obviously this estimate is correlated to the collection point, because for a given ϕ, if the mass deposited in the proximal area increases, it decreases in the distal one, since the total mass deposited conserves. The highest values of the simulated tephra mass by both models are identified in SP59 in Milo (values of 2750-3375 kg with Tephra2 and 3000-4250 kg with Fall3D are accumulated at the end of the paroxysms sequence), that is the nearest point to

300   Etna summit among those analysed (far away about 12 km), in contrast with the calculated ash load in SP92 in Zafferana Etnea (about 725-800 kg with Tephra2 and 250-450 kg are accumulated at the end of the paroxysms sequence with Fall3D), a point that is also among the nearest to Etna among those analysed (12.2 km), but located more southward respect to Milo. We can evaluate these results taking into account the tolerance boundaries, usually considered as more/less five times the estimated values (Scollo et al., 2007). Indeed, the variability of tephra mass for all the road-points computed with Tephra2

305   ranges between limit values of 750-3375 kg, whereas the variability derived from Fall3D is between 250-4250 kg. The time-cumulative function derived from Tephra2 presents larger steps in concomitance with events of 14 March, 22 and 28 May, 1 July 2021 for SP59 in Milo, E45, SP49 and SS114 in Santa Venerina and SP8 in Zafferana Etnea whereas E45 and SS114 in Milo show a larger step during the event on 24 May 2021. During the other events, the tephra mass is not large enough to generate major steps in the time-cumulative function. For most road-points, the total accumulated tephra mass stabilises at

310   values between 500 kg and 1250 kg after the paroxysm of 20 July 2021, with the exception of SP59 in Milo. The time-cumulative function obtained with Fall3D shows larger steps during the events of 28 May, 2 and 27 June, 31 July 2021 for SP59 in Milo. E45 and SS114 in Milo show a larger step on 27 June 2021, whereas SP41, E45 and SS114 in Santa Venerina exhibit a large step on 29 August 2021, and SP92 in 17 June 2021.

In Zafferana Etnea, SP8 shows a time increase of tephra mass, whereas in Zafferana Etnea the tephra mass is constant at
315   values between 250 kg and 500 kg by the end of June. The time-cumulated tephra mass on SP41, E45 and SS114 in Santa
Venerina and SS114 on Milo stabilises between 1325 kg and 2075 kg starting from the beginning of August. Also in the case
of Fall3D, SP59 in Milo is confirmed as the most impacted road-point to the accumulation of tephra in time where the time-
cumulated tephra increases more than at the other target points, with larger steps, and then stabilises starting from August.
These results suggest that, following the 2021 cluster of Etna lava fountains, the roads of Milo and Santa Venerina
320   municipalities have been the most impacted from tephra deposition in time.
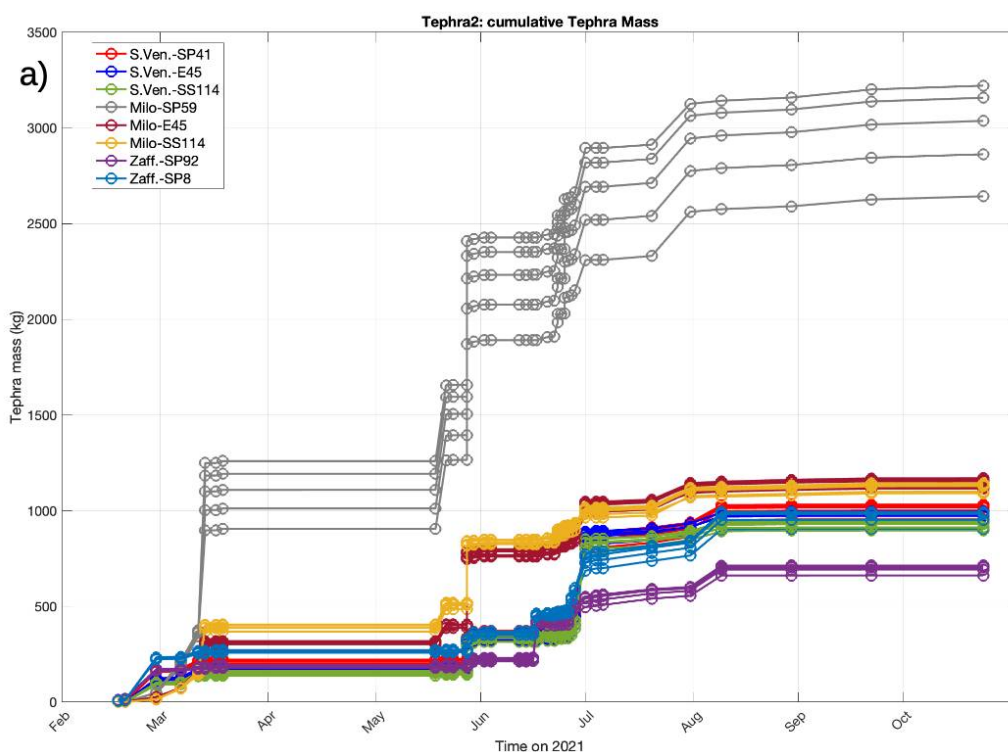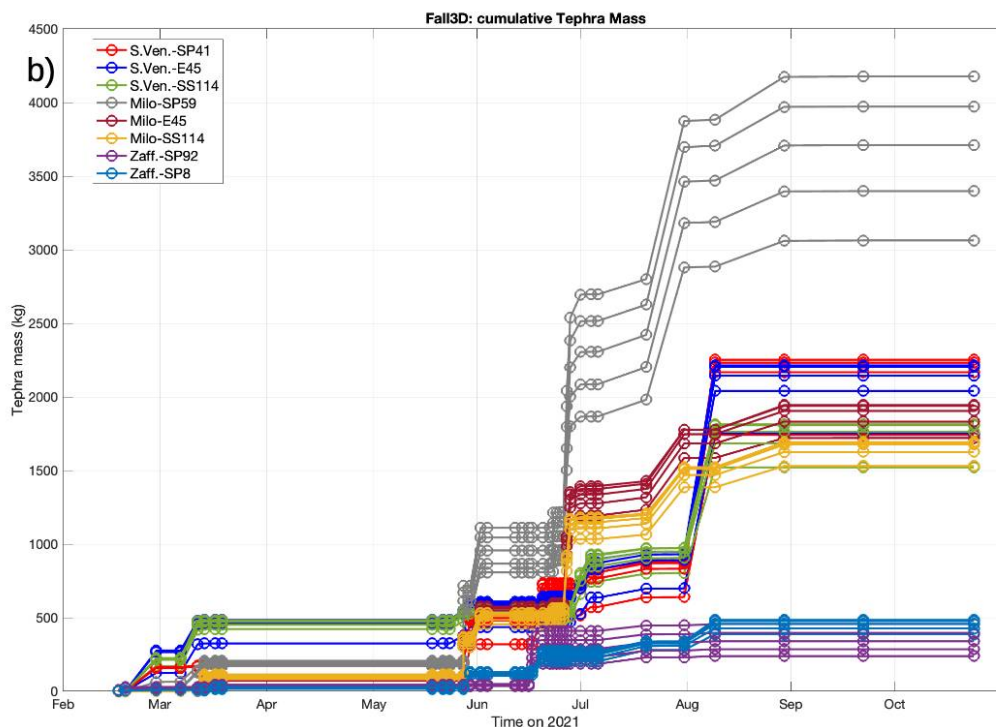
Figure 4: Time series of the time-cumulative tephra mass simulated by the Tephra2 (a) and Fall3D (b) models for all the analysed Etna explosive events in 2021 having a plume dispersal toward east and south east. Each road-point is identified by a different coloured line. For each road-point, we plot the cumulative tephra mass for each median value of φ. The larger the mean grain size, the higher the accumulated load for that road-point.

3.3 Total mass accumulated on selected roads

In this section we quantify the total tephra mass deposited on selected main roads previously listed in Table 3 for each municipality. Figure 5.a, 5.b and 5.c are related, respectively, to the time-cumulative mass on Milo (a), Santa Venerina (b) and Zafferana Etnea (c) computed on selected roads of known area. Analysing the panels in Fig. 5 we observe some rapid increases in the cumulative trend of tephra mass mainly for the Fall3D simulations (grey dashed line) with respect to Tephra2 (dark continuous line) simulations. These rapidly increasing trends are found in Milo on 12 March, 28 May (18:10-21:10 UTC), 27 June 2021, in Santa Venerina on 30 May, 17 June 2021 and in Zafferana Etnea. Generally, all the selected roads show a large step in the estimated cumulative tephra mass on 19 February, regardless of the model used. The largest step of total mass is found around June and July, as confirmed by the plots shown in Fig. 5.a.

16
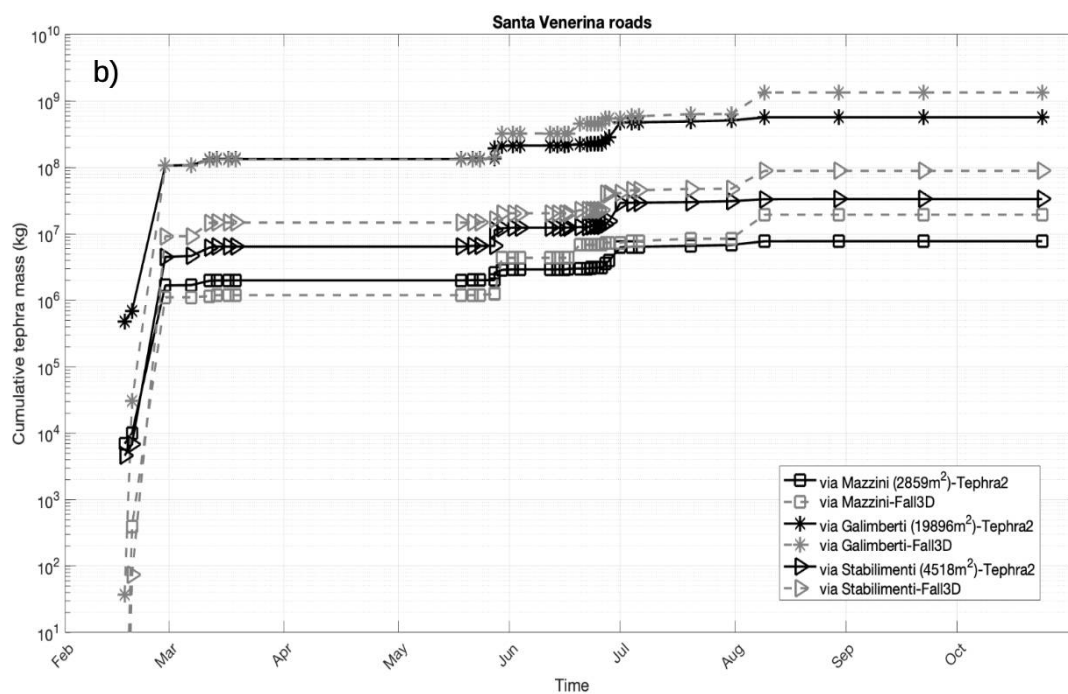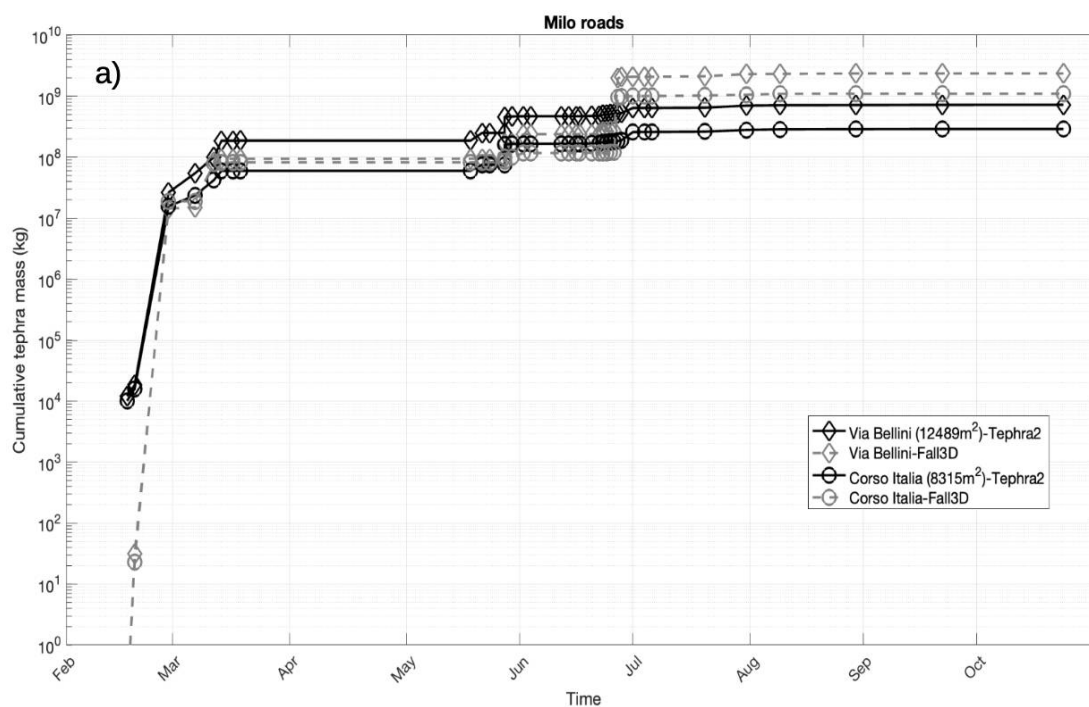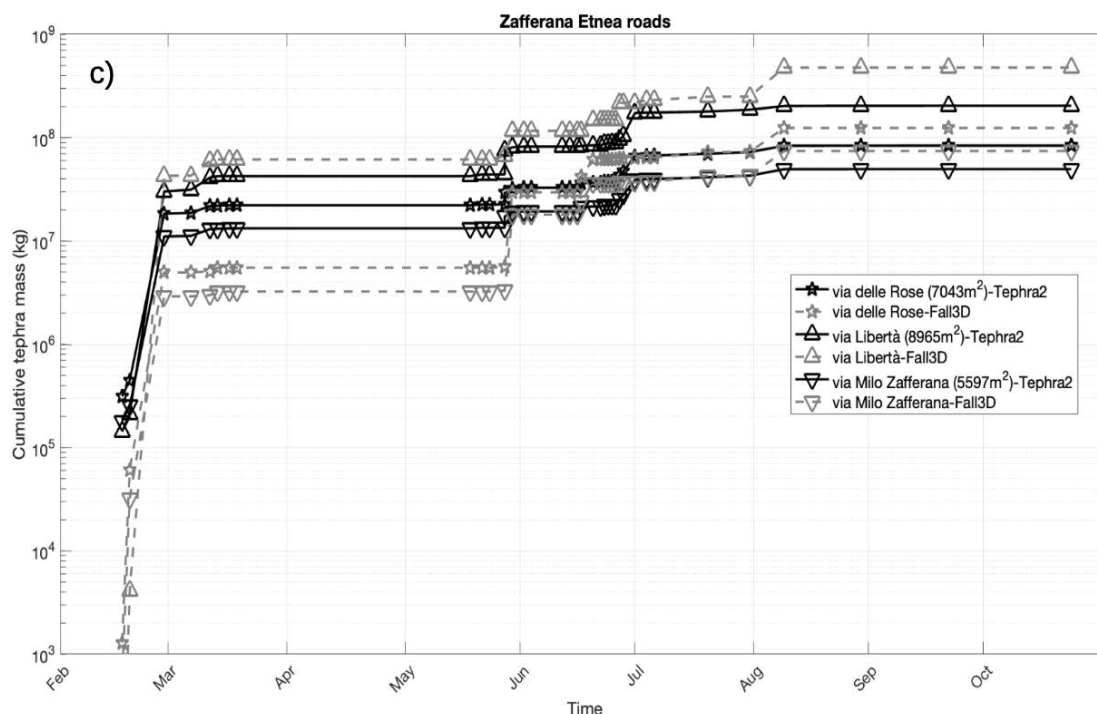
Figure 5: Cumulative tephra mass on selected roads for Milo (a), Santa Venerina (b) and Zafferana Etnea (c), respectively, for all Etna lava fountains here analysed and simulated using the Tephra2 (dark continuous line) and Fall3D (grey dashed line) models. Each road is plotted with different symbols and identified by the relative area (m²), as listed in the legend.

In Table 4 we summarise the total tephra mass deposited during the whole series of 39 Etna events in 2021 for the selected roads in each municipality, whereas the last three rows show the total tephra mass computed for the complete road network of each town. The Fall3D estimates are generally greater than Tephra2 ones, although within the variability of more/less five times. We observe that during about one year of Etna's paroxysms, in the nearest municipalities under examination, the estimated value of total tephra mass accumulated in the main streets ranges between 10^6-10^9 kg. A difference of at most one order of magnitude in the total accumulated mass according to the two models is found. It is worth noting that these values are computed under the worst condition, i.e. without considering the tephra mobilisation due to external factors, such as rain or wind, during the complete time range, as well as assuming not road cleaning after each event. Therefore, this tephra mass represents a computed estimate of the total amount of tephra mass that theoretically had to be removed to the roads and disposed of during and after the 2021 crisis.

Table 4. Total mass accumulated over 39 Etna events on the selected roads for Milo, Santa Venerina and Zafferana Etnea municipalities, as simulated by Tephra2 and Fall3D models (fixing φ=0.5). The total mass on the whole road network of Milo, Santa Venerina and Zafferana is in the last three rows.

39 Etna lava fountains on 2021	Mass (10^7 kg)	
Location	Tephra2	Fall3D
Milo-Via V. Bellini	72.2	235.9
Milo-Corso Italia	29.0	109.9
S. Venerina-Via G. Mazzini	0.8	1.9
S. Venerina-Via D. Galimberti	57.2	135.0
S. Venerina-Via Stabilimenti	3.4	8.9
Zafferana E.-Via Libertà	8.4	12.4
Zafferana E.-Via Zafferana Milo	20.4	47.7
Zafferana E.-Via delle Rose	5.0	7.4
Total mass on the whole road network of each municipality (10^7 kg)		
Milo	7975.3	16295.5
Santa Venerina	878.7	2882.1
Zafferana Etnea	5631.5	29053.5

3.4 Total mass accumulated on full road network

Similarly to what is shown in Fig. 3, Figure 6 shows the cumulative tephra load (kg/m^2) on the geo-referenced road map within the Milo (light orange area), Santa Venerina (light pink area) and Zafferana Etnea (light green area) municipalities for 360 all 39 Etna lava fountains, computed using Tephra2 (Fig. 6.a)) and Fall3D (Fig. 6.b)) models.
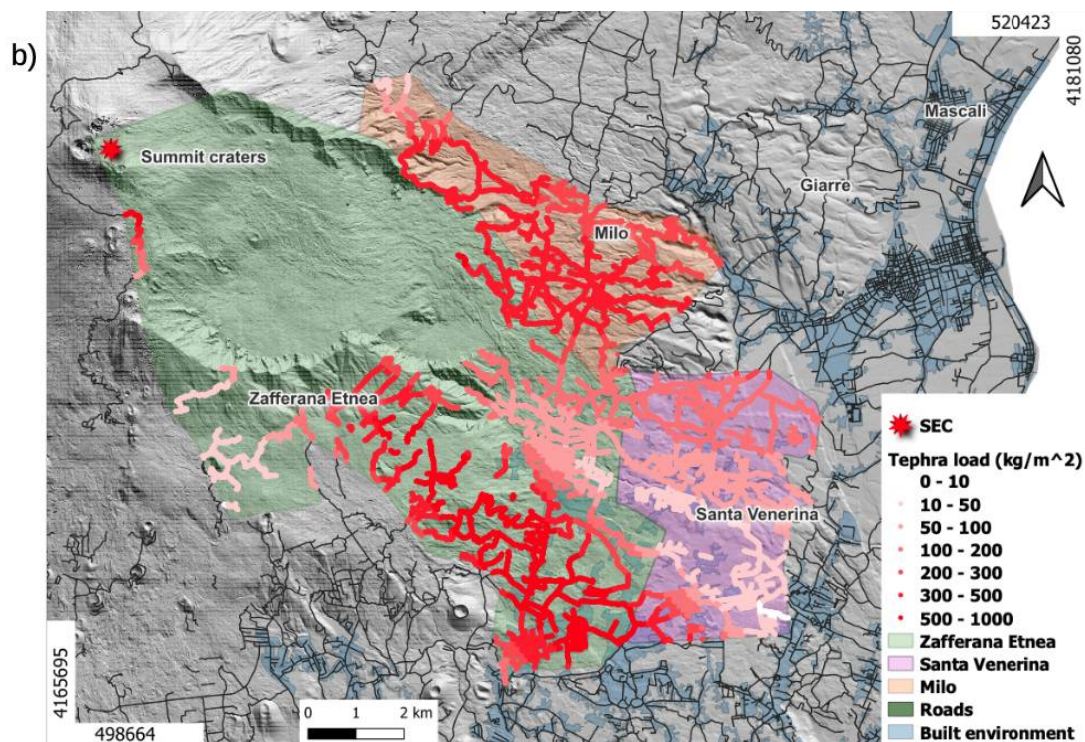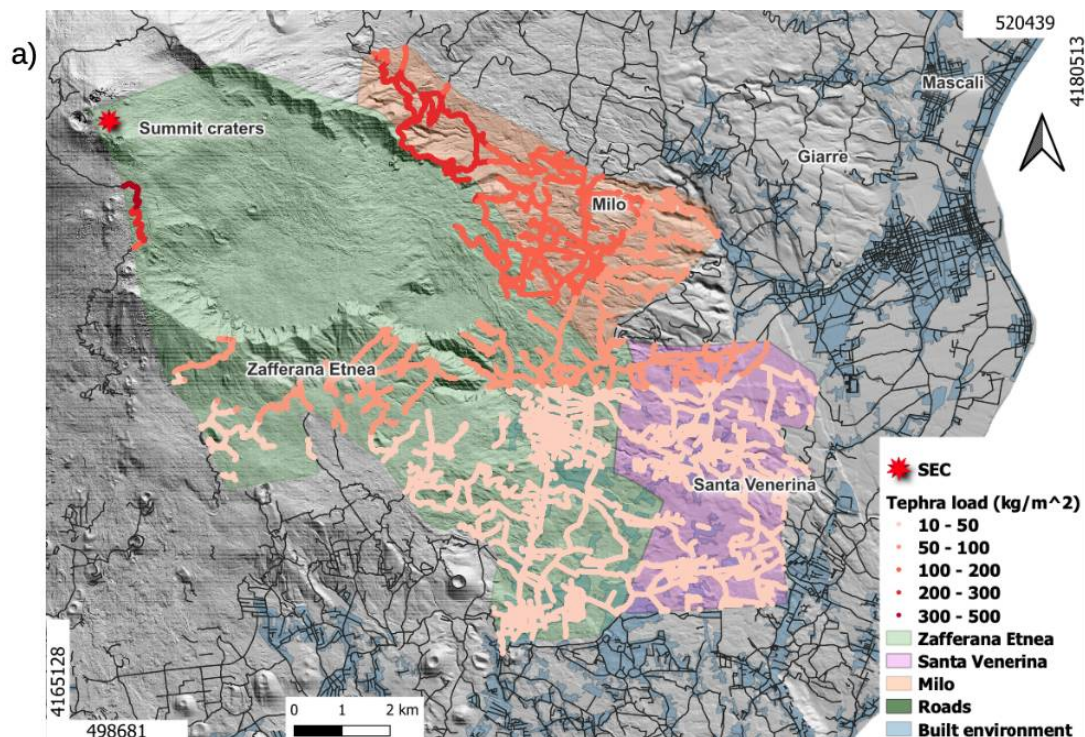
Figure 6: Cumulative tephra load (kg/m²) for all 39 Etna lava fountains analysed in this work, computed on the whole road
365   **network of Milo, Santa Venerina and Zafferana Etnea using (a) Tephra2 and (b) Fall3D models, assuming a ϕ=0.5. The road**
graph is bold highlighted and in red scale coloured in function of deposited tephra values. Georeferenced map of road network
(dark lines) of the Etna volcano area (shapefiles with the road data is publicly available from the Regione Sicilia website:
https://www.regione.sicilia.it/). Made with QGIS.

Considering the area of each road, we compute the time-cumulative tephra mass (kg) relative to Milo, Santa Venerina and
370   Zafferana, over the whole road network, as computed by both numerical models (Fig. 7). Normally, the cumulative tephra
mass derived from Tephra2 (dark continuous line) after an initial rapid growth tends to stabilise, in contrast with the trends
obtained using Fall3D (grey dashed line), which present rapid increases in estimates throughout the sequence. These leaps in
Milo are for the events on 28 May, 23 June (17:40-19:00 UTC) and 27 June 2021, in Santa Venerina on 28 February, 23 and
27 June 2021 and in Zafferana Etnea on 28 February and 17 June 2021. The maximum value of tephra mass deposited on the
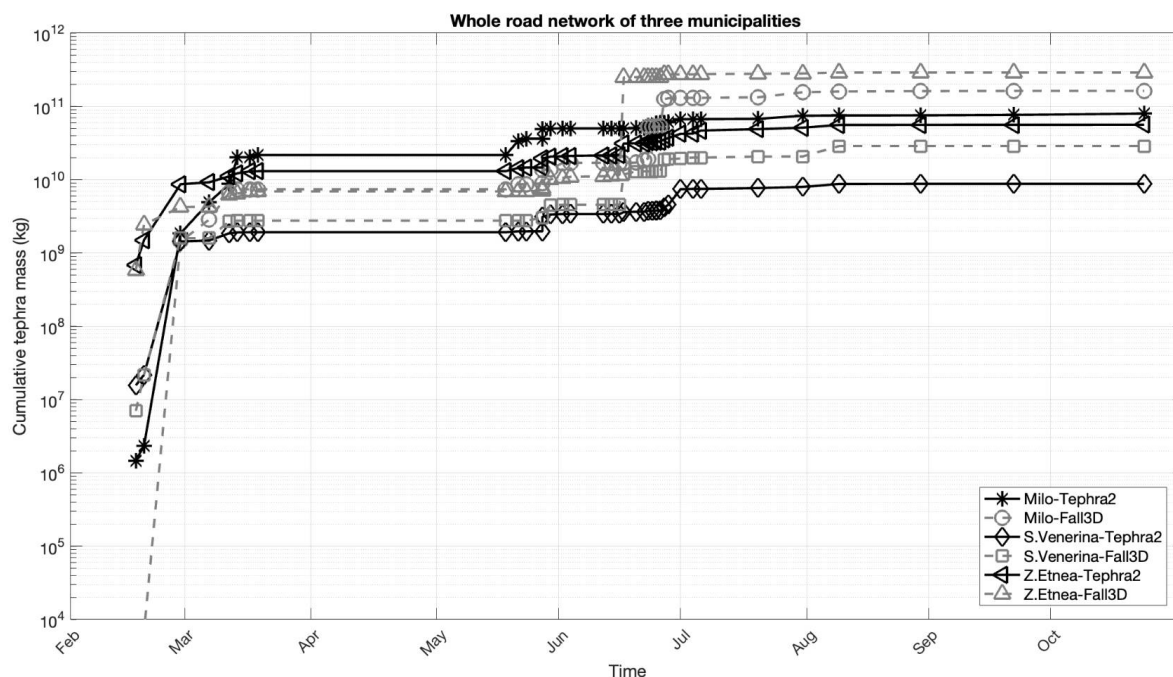375   whole road network in the three municipalities ranges between 10^{10} to 10^{12} kg.

Figure 7: Cumulative tephra mass for all the 2021 Etna lava fountains analysed in this work, simulated using Tephra2 (dark
continuous line) and Fall3D (grey dashed line) models, for the whole road network in Milo, Santa Venerina and Zafferana Etnea.

2 Discussion and conclusions

Considering the question about the quantification of the total tephra mass deposited in a given infrastructure of interest following an (or a series of) explosive volcanic eruptions, in this work we assessed, for the first time, the cumulated tephra mass on the road networks in three selected towns on Etna's eastern flank during several paroxysms that occurred in the year 2021. This cumulated mass is a theoretical estimate of the amount of material that had to be removed from the roads and disposed of during the 2021 volcanic activity. We have focussed on three target municipalities located on the east flank, i.e. Milo, Santa Venerina and Zafferana Etnea. According to the law at the time of the eruption, such material had to be handled and disposed of as special waste (Art. 35 decreto legge 77/2021); at the time of writing this paper a new law allows the use of this material for other purposes (DA n.8/Gab. 22/04/2024, https://www.regione.sicilia.it) as, for example, building construction. In this perspective, this work is a first attempt to estimate the amount of tephra that must be removed during a crisis and could be reused instead of disposed, converting in this way a potential problem into an opportunity.

Processing measurements derived from visible and thermal cameras of INGV-OE, and, when available, from SEVIRI images and the XWR data, we can retrieve the main ESPs, useful inputs to run numerical models. In this way we can simulate and evaluate the cumulated tephra load on roads in time, focusing on the three target municipalities. Processing these results with the QGIS tool, we are able to identify the roads more exposed to tephra deposition. We consider that the results of this analysis can be a valuable source of information to support the management of volcanic crises and for planning the reinstatement of road networks after a crisis.

It is known that effective and realistic transport management strategies are essential into volcanic contingency planning in sectors where key infrastructure are at risk, such as the road networks. Evaluating tephra mass using two (or more) different models allows assessing epistemic uncertainty, to estimate the different sensitivity of each model to same input ESPs and the variability of the median ϕ. It is worth highlighting that we have neglected the uncertainties in the ESP's values (such as Q_M, TEM and H_{TP}), even though they are affected by intrinsic uncertainty due to pre- and post-elaboration of data, to the instrument sensitivity and accuracy, which can significantly affect the model outputs (see e.g., Mereu et al, 2023). This can lead to larger uncertainties in the simulated tephra load in addition to those mainly due both to the different model settings and the physical assumptions implemented in each numerical model.

In this work we are not considering the effect of rain which can remain trapped in the tephra deposit. Furthemore, depending on the rain's intensity, the road traffic safety can worsen (e.g., by making the transport network particularly slippery) or can be improved (e.g, by washing the road surface from the ash deposit). Specific thresholds of tephra load that can damage the main roads system, and the necessary actions to mitigate the tephra effects are defined and known in the literature (e.g. Jenkins et al. 2015; Bonadonna et al. 2021; Table 8 in Bonadonna et al., 2023).

As a final consideration, we point out the importance of the validation of the results of tephra load simulation obtained with two different numerical models by comparing their output with ground sampling data (available from Pardini et al., 2023) as well as with the XWR retrievals for the Etna explosive activity on February 28, 2021. The tephra deposit estimations, as

22

listed in Table 2, highlight the good agreement among the ground sampling, XWR retrievals and the output of numerical models. This observation makes us confident to use the two different models in evaluating not only qualitatively but also

415 quantitatively the tephra deposited during recent Etna paroxysms. In this way it's possible to provide plausible values of ground-cumulated tephra mass on roads, and identify which routes in the road network of the target towns may be most impacted in next eruptions. Moreover, these results may support decision makers in different ways e.g. for planning and consequently for better management of a future volcanic crisis due to explosive activity of Etna volcano, as well as for getting valuable information about the order of magnitude of the total mass of tephra available for planning the subsequent

420 disposal and/or reuse.

Author contributions: MP and MS performed the simulations; LM analyzed the data; LM wrote the manuscript draft; LM, AG, SS, LS, CB, MP and MS reviewed and edited the manuscript; AG ans SS funding acquisition.

425 **Competing interests:** The authors declare that they have no conflict of interest

References

Ágústsdóttir, A. M.: Ecosystem approach for natural hazard mitigation of volcanic tephra in Iceland: building resilience and sustainability. Nat. Hazards 78, 1669–1691. doi: 10.1007/s11069-015-1795-6, 2015.

435 Andronico, D.; Cannata, A.; Di Grazia, G.; Ferrari, F.: The 1986–2021 paroxysmal episodes at the summit craters of Mt. Etna: Insights into volcano dynamics and hazard. Earth-Sci. Rev., 220, 103686, 2021.

Barsotti, S., Di Rienzo. D.I., Thordarson, T., Björnsson, B.B. and Karlsdóttir S.: Assessing Impact to Infrastructures Due to Tephra Fallout From Öræfajökull Volcano (Iceland) by Using a Scenario-Based Approach and a Numerical Model, Front. Earth Sci. 6:196. doi: 10.3389/feart.2018.00196., 2018.

440 Baxter., P.: Medical effects of volcanic eruptions, Bull. Volcanol. (1990) 52, 532. doi: 10.1007/BF00301534., 1990.

Horwell, C. J., and Baxter, P. J.: The respiratory health hazards of volcanic ash: a review for volcanic risk mitigation, Bull. Volcanol. 69, 1–24. doi: 10.1007/ s00445- 006- 0052- y, 2006.

Bebbington, M., Cronin, S. J., Chapman, I., and Turnera, M. B.: Quantifying volcanic ash fall hazard to electricity infrastructure. J. Volcanol. Geother. Res. 177:4. doi: 10.1016/j.jvolgeores.2008.07.023, 2008.

https://doi.org/10.5194/egusphere-2024-2028
Preprint. Discussion started: 25 July 2024
© Author(s) 2024. CC BY 4.0 License.

445   Biass S., Bonadonna C., Traglia F. et al: Probabilistic evaluation of the physical impact of future tephra fallout events for the Island of Vulcano, Italy. Bull Volcanol 78:1–22. https://doi.org/10.1007/ s00445-016-1028-1, 2016.

Biass, S., Todde A., Cioni R., Pistolesi M., Geshi N., Bonadonna C.: Potential impacts of tephra fallout from a large-scale explosive eruption at Sakurajima volcano, Japan, Bull Volcanol 79:73 DOI 10.1007/s00445-017-1153-5, 2017.

Blake, D.M.; Wilson, T.M.; Gomez, C.: Road marking coverage by volcanic ash. Environ. Earth Sci. 75, 1–12, 2016.

450   Blake, D. M., Wilson T. M., Cole J. W., Deligne N. I. and Lindsay, J. M.: Impact of Volcanic Ash on Road and Airfield Surface Skid Resistance, Sustainability 2017, 9, 1389; doi: 10.3390/su9081389, 2017.

Blong, R.J. Volcanic Hazards: A Sourcebook on the Effects of Eruptions; Academic Press Inc.: Sydney, Australia, 1984.

Blong, R. J.: Volcanic hazards risk assessment, Monitoring and Mitigation of Volcano Hazards, eds R. Scarpa and R. I. Tilling (Berlin: Springer), 1996.

455   Bonadonna, C., C. B. Connor, B. F. Houghton, L. Connor, M. Byrne, A. Laing, and T. K. Hincks: Probabilistic modeling of tephra dispersal: Hazard assessment of a multiphase rhyolitic eruption at Tarawera, New Zealand, J. Geophys. Res., 110, B03203, doi:10.1029/2003JB002896, 2005.

Bonadonna, C.: Probabilistic modelling of tephra dispersal, in: Statistics in Volcanology, edited by: Mader, H., Cole, S., and Connor, C. B., IAVCEI Series, Volume 1, Geological Society of London, 2006.

460   Bonadonna C, Frischknecht C, Menoni S, Romerio F, Gregg CE, Rosi M, Biass S, Asgary A, Pistolesi M, Guobadia D., Gattuso A., Ricciardi A, Cristiani C.: Integrating hazard, exposure, vulnerability and resilience for risk and emergency management in a volcanic context: the ADVISE model, Journal of Applied Volcanology, 2021a

Bonadonna C, Biass S, Menoni S, Chris EG: Assessment of risk associated with tephra-related hazards, In: Papale, P (Ed.). Forecasting and Planning for Volcanic Hazards, Risks, and Disasters: Elsevier, 329-378. (Hazards and Disasters), 2021b

465   Calvari, S.; Cannavò, F.; Bonaccorso, A.; Spampinato, L.; Pellegrino, A.G.: Paroxysmal Explosions, Lava Fountains and Ash Plumes at Etna Volcano: Eruptive Processes and Hazard Implications. Front. Earth Sci. 6, 107, https://doi.org/10.3389/feart.2018.0010.7, 2018.

Calvari, S.; Biale, E.; Bonaccorso, A.; Cannata, A.; Carleo, L.; Currenti, G.; Di Grazia, G.; Ganci, G.; Iozzia, A.; Pecora, E.; et al.: Explosive Paroxysmal Events at Etna Volcano of Different Magnitude and Intensity Explored through a

470   Multidisciplinary Monitoring System. Remote Sens., 14, 4006, https://doi.org/10.3390/rs14164006, 2022(a).

Calvari, S.; Nunnari, G.: Comparison between Automated and Manual Detection of Lava Fountains from Fixed Monitoring Thermal Cameras at Etna Volcano, Italy. Remote Sens., 14, 2392. https://doi.org/10.3390/rs14102392, 2022 (b).

Casadevall, T. J.: The 1989–1990 eruption of redoubt volcano, Alaska: impacts on aircraft operations, J. Volcanol. Geother. Res. 62, 301–316. doi: 10.1016/0377- 0273(94)90038- 8, 1994.

475   Connor, L. G. and Connor, C. B.: Inversion is the key to dispersion: Understanding eruption dynamics by inverting tephra fallout, in: Statistics in Volcanology, Society for Industrial and Applied Mathematics, Special Publication of IAVCEI N. 1, Mader, H., Cole, S., and Connor, C. B., 231–242, Geological Society, London, 2006.

Corradini, S., Guerrieri, L., Lombardo, V., Merucci, L., Musacchio, M., Prestifilippo, M., Scollo, S., Silvestri, M., Spata, G., Stelitano, D (2018). Proximal monitoring of the 2011-2015 Etna lava fountains using MSG-SEVIRI data. Geosciences 2018, 8, 140

480

Costa A., G. Macedonio a, A. Folch: A three-dimensional Eulerian model for transport and deposition of volcanic ashes, Earth and Planetary Science Letters 241, 634–647, 2006.

Costa, A., Folch, A., Macedonio, G., Giaccio, B., Isaia, R., and Smith, V. C.: Quantifying volcanic ash dispersal and impact of the Campanian Ignimbrite super-eruption, Geophysical Research Letters, 39, https: //doi.org/10.1029/2012GL051605,

485 2012.

Dominguez L, Bonadonna C, Frischknecht C, Menoni S and Garcia A (2021) Integrative Post-event Impact Assessment Framework for Volcanic Eruptions: A Disaster Forensic Investigation of the 2011–2012 Eruption of the Cordón Caulle Volcano (Chile). Front. Earth Sci. 9:645945. doi: 10.3389/feart.2021.645945

Folch A., Costa A, Macedonio G.: FALL3D: A computational model for transport and deposition of volcanic ash.

490 Computers and Geosciences 35, 1334–1342, 2009.

Folch, A., Mingari, L., Gutierrez, N., Hanzich, M., Macedonio, G. and Costa, A.: FALL3D-8.0: a computational model for atmospheric transport and deposition of particles, aerosols and radionuclides – Part 1: Model physics and numerics, https://doi.org/10.5194/gmd-13-1431, 2020

Gordon, K.D.; Cole, J.W.; Rosenberg, M.D.; Johnston, D.M.: Effects of volcanic ash on computers and electronic

495 equipment. Nat. Hazards, 34, 231–262, 2005.

Guffanti, M., Mayberry, G. C., and Casadevall, T. J.: Volcanic hazards to airports. Nat. Hazards 51, 287–302. doi: 10.1007/s11069-008-9254-2, 2009.

Guobadia, D., Gattuso, A., Ricciardi, A. and Cristiani, C., Integrating hazard, exposure, vulnerability and resilience for risk and emergency management in a volcanic context: the ADVISE model, J. Appl. Volcanol. (2021) 10:7

500 https://doi.org/10.1186/s13617-021-00108-5

Hayes, J.L., Biass, S., Jenkins, S.F. et al. Integrating criticality concepts into road network disruption assessments for volcanic eruptions. J Appl. Volcanol. 11, 8 (2022). https://doi.org/10.1186/s13617-022-00118-x

Heiken, G.; Murphy, M.; Hackett, W.; Scott, W.: Volcanic Hazards to Energy Infrastructure-Ash Fallout Hazards and Their Mitigation; World Geothermal Congress: Florence, Italy, pp. 2795–2798,1995.

505 Horwell, C.J. and Baxter, P. (2006) The Respiratory Health Hazards of Volcanic Ash: A Review for Volcanic Risk Mitigation. Bulletin of Volcanology, 69, 1-24. http://dx.doi.org/10.1007/s00445-006-0052-y

Jenkins SF, Spence RJS, Fonseca JFBD, Solidum RU, Wilson TM (2014) Volcanic risk assessment: quantifying physical vulnerability in the built environ- ment. J Volcanol Geotherm Res 276:105–120

Jenkins, S., Barsotti, S., Hincks, T. K., Neri, A., Phillips, J. C., Sparks, R. S. J., et al.: Rapid emergency assessment of ash

510 and gas hazard for future eruptions at Santorini Volcano, Greece. J. Appl. Volcanol. Soc. Volcanoes 20154:16. doi: 10.1186/s13617-015-0033-y, 2015.

Johnston, D.M.; Daly, M.: Auckland erupts!!, N. Z. Sci. Mon. 1995, 8, 6–7, 1995.

Johnston, D.M.: Physical and Social Impacts of Past and Future Volcanic Eruptions in New Zealand. Ph.D. Thesis, Massey University, Palmerston North, New Zealand, 1997.

515 Labadie, J.R.: Volcanic Ash Effects and Mitigation. Adapted from a Report Prepared in 1983 for the Air Force Office of Scientific Research and the Defence Advanced Research Projects Agency, 1994.

Marzano, F. S., Picciotti, E., Vulpiani, G., Montopoli, M.: Synthetic signatures of volcanic ash cloud particles from X-band dual-polarization radar. IEEE Transactions on Geoscience and Remote Sensing, 50(1), 193–211. https://doi.org/10.1109/TGRS.2011.2159225, 2012.

520 Marzano, F. S., Mereu, L., Scollo, S., Donnadieu, F., Bonadonna, C.: Tephra mass eruption rate from ground-based X-band and L-band microwave radars during the November 23, 2013 Etna Paroxysm. IEEE Transactions on Geoscience and Remote Sensing, 58(5), 3314–3327. https://doi.org/10.1109/tgrs.2019.2953167, 2020.

Mastin, L. G., Guffanti, M., Servranckx, R., Webley, P., Barsotti, S., Dean, K., et al.: A multidisciplinary effort to assign realistic source parameters to models of volcanic ash-cloud transport and dispersion during eruptions. Journal of
525 Volcanology and Geothermal Research, 186(1–2), 10–21, https://doi.org/10.1016/j.jvolgeores.2009.01.008, 2009.

Mereu, L., Marzano, F. S., Montopoli, M., Bonadonna, C.: Retrieval of tephra size spectra and mass flow rate from C-band radar during the 2010 Eyjafjallajökull eruption, Iceland. IEEE Transactions on Geoscience and Remote Sensing, 53(10), 5644–5660. https://doi. org/10.1109/tgrs.2015.2427032, 2015.

Mereu, L., Scollo, S., Bonadonna, C., Freret-Lorgeril, V., Marzano, F. S.: Multisensor characterization of the incandescent
530 jet region of lava fountain-fed tephra plumes. Remote Sensing, 12(21), 3629. https://doi.org/10.3390/rs12213629, 2020.

Mereu, L., Scollo, S., Bonadonna, C., Donnadieu, F., Freret Lorgeril, V., Marzano, F. S.: Ground-based remote sensing of volcanic mass flow: Retrieval techniques and uncertainty analysis of Mt. Etna eruptions in 2015. IEEE Journal of Selected Topics in Applied Earth Observations and Remote Sensing, 15, 504–518. https://doi.org/10.1109/jstars.2021.3133946, 2022.

Mereu, L., Scollo, S., Garcia, A., Sandri, L., Bonadonna, C., Marzano, F. S.: A new radar-based statistical model to quantify
535 mass eruption rate of volcanic plumes. Geophysical Research Letters, 50, e2022GL100596, https://doi. org/10.1029/2022GL100596, 2023.

Miller, T.P.; Casadevall, T.J.: Volcanic ash hazards to aviation. In Encyclopedia of Volcanoes, 1st ed.; Sigurdsson, H., Houghton, B., Rymer, H., Stix, J., McNutt, S., Eds.; Academic Press: San Diego, CA, USA, pp. 915–930, 1999.

Montopoli, M.: Velocity profiles inside volcanic clouds from three-dimensional scanning microwave dual-polarization
540 Doppler radars. Journal of Geophysical Research: Atmospheres, 121(13), 7881–7900. https://doi.org/10.1002/2015JD023464, 2016.

Macedonio G., Costa A.: Brief Communication "Rain effect on the load of tephra deposits", Natural Hazards and Earth System Science 12(4):1229– 1233, 2012

545 Pardini F., De' Michieli Vitturi M., Andronico D., Esposti Ongaro T., Cristaldi A. and Neri A.: Real-time probabilistic assessment of volcanic hazard for tephra dispersal and fallout at Mt. Etna: the 2021 lava fountain episodes, Bulletin of Volcanology, 85:6 https://doi.org/10.1007/s00445-022-01614-z, 2023.

Romeo, F.; Mereu, L.; Scollo, S.; Papa, M.; Corradini, S.; Merucci, L.; Marzano, F.S.: Volcanic Cloud Detection and Retrieval Using Satellite Multisensor Observations. RemoteSens.,15,888. https:// doi.org/10.3390/rs15040888, 2023.

Sarna-Wojcicki, A.M.; Shipley, S.; Waitt, R.B.; Dzurisin, D.; Wood, S.H.: Areal distribution, thickness, mass, volume, and
550 grain size of air-fall ash from the six major eruptions of 1980. In The 1980 Eruptions of Mount Saint Helens; USGS Numbered Series 1250; Lipman, P.W., Mullineaux, D.R., Eds.; U.S. Government Publishing Office: Washington, DC, USA, pp. 577–600, 1981.

Scollo, S., Del Carlo, P., Coltelli, M., Tephra fallout of 2001 Etna flank eruption: Analysis of the deposit and plume dispersion, Journal of Volcanology and Geothermal Research Volume 160, Issues 1–2, 1 February 2007, Pages 147-164,
555 https://doi.org/10.1016/j.jvolgeores.2006.09.007

Scollo, S., S. Tarantola, C. Bonadonna, M. Coltelli, and A. Saltelli: Sensitivity analysis and uncertainty estimation for tephra dispersal models, J. Geophys. Res., 113, B06202, doi:10.1029/2006JB004864, 2008.

Scollo, S., Prestifilippo, M., Spata, G., D'Agostino, M., Coltelli, M.: Monitoring and forecasting Etna volcanic plumes. Natural Hazards and Earth System Sciences, 9(5), 1573–1585. https://doi.org/10.5194/nhess-9-1573, 2009.

560 Scollo, S., M. Coltelli, C. Bonadonna, and P. Del Carlo: Tephra hazard assessment at Mt. Etna (Italy), Nat. Hazards Earth Syst. Sci., 13, 3221–3233, doi:10.5194/nhess-13-3221-2013, 2013.

Scollo S., Prestifilippo M., Bonadonna C., Cioni R., Corradini S., Degruyter W., Rossi E., Silvestri M., Biale E., Carparelli G., Cassisi C., Merucci L., Musacchio M. and Pecora E.: Near-Real-Time Tephra Fallout Assessment at Mt. Etna, Italy, Remote Sens., 11, 2987; doi:10.3390/rs11242987, 2019.

565 Spence, R. J. S., Kelman, I., Baxter, P. J., Zuccaro, G., and Petrazzuoli, S.: Residential building and occupant vulnerability to tephra fall, Natur. Hazards Earth Syst. Sci. 5, 477–494. doi: 10.5194/nhess-5-477-2005.

Volentik A.C.M., Connor C.B., Connor L.J., Bonadonna C.: Aspects of volcanic hazards assessment for the Bataan nuclear power plant, Luzon Peninsula, Philippines. In: Connor C., Chapman N.A., Connor L. (eds) Volcanic and tectonic hazard assessment for nuclear facilities. Cambridge University Press, Cambridge, 2009.

570 Vulpiani, G., Ripepe, M., Valade, S.: Mass discharge rate retrieval combining weather radar and thermal camera observations. Journal of Geophysical Research: Solid Earth, 121(8), 5679–5695. https://doi.org/10.1002/2016jb013191, 2016.

Wardman, J. B., Wilson, T., Bodger, P. S., Cole, J. W., and Johnston, D. M.: Investigating the electrical conductivity of volcanic ash and its effects on HV power systems. Phys. Chem. Earth 45–46, 128–145. doi: 10.1016/j.pce.2011.09.003, 2012
575 Wilson, T. M, Stewart, C., Sword-Daniels, V., Leonard, G. S., Johnston, D. M, Cole, J. W., Wardman, J., et al.: Volcanic ash impacts on critical infrastructure. Phys. Chem. Earth 45–46, 5–23. doi: 10.1016/j.pce.2011.06.006, 2012.

Wilson, G.; Wilson, T.M.; Deligne, N.I.; Cole, J.W.: Volcanic hazard impacts to critical infrastructure: A review. J. Volcanol. Geotherm. Res., 286, 148–182, 2014.

Magill, C., Blong, R. and McAneney, J., VolcaNZ - A volcanic loss model for Auckland, New Zealand, Journal of Volcanology and Geothermal Research 149 (2006) 329–345.

Hayes, J. L., Wilson, T. M. and Magill, C., Tephra fall clean-up in urban environments, Journal of Volcanology and Geothermal Research 304 (2015) 359–377.